**Title**

Prediction of the Hydrodynamic Loads on a Full-Scale Caisson at High Reynolds Number

**Permalink**

https://escholarship.org/uc/item/6qj0j6zb

**Journal**

Journal of Structural Engineering, 149(6)

**ISSN**

0733-9445

**Authors**

Niu, Yanwei
Younis, Bassam A

**Publication Date**

2023-06-01

**DOI**

10.1061/jsendh.steng-11841

**Copyright Information**

Peer reviewed

# Prediction of the Hydrodynamic Loads on a Full-Scale Caisson at High Reynolds Number

Yanwei Niu[1] and Bassam A. Younis[2]

**Abstract:** The paper reports on the computation of the hydrodynamic loads on a full-scale caisson at high Reynolds number in the presence of vortex shedding. The objective was to obtain reliable predictions of the resulting mean and fluctuating forces to guide the design of an actual caisson in the absence of relevant experimental data. A further objective was to investigate the effectiveness of alternative methods for the control of vortex shedding that can be implemented in practice. Two such methods were evaluated: (1) by rounding the corners of the rectangular-sectioned caisson, and (2) by the placement of a splitter plate in the separated wake region. The computations, which were performed using the OpenFOAM open-source software, were for a fixed caisson and hence did not account for motions due to vortex-induced vibrations. The effects of turbulence were accounted for by performing large-eddy simulations, and by using two-equation eddy-viscosity closures, one of which was specifically adapted to account for the interactions between the periodic vortex shedding and the random turbulence. The numerical accuracy was checked using the grid convergence index method, and the computations were extensively validated against data from relevant benchmark flows. The recommendations of this research were implemented in the design of a full-scale caisson that has since been deployed in a bridge construction project. **DOI: 10.1061/JSENDH.STENG-11841.** © *2023 American Society of Civil Engineers.*

**Author keywords:** Full-scale caisson; Turbulence modeling; Large-eddy simulations; Flow control; Vortex shedding.

## Introduction

The ever-growing demand for the construction of mega infrastructures in deep waters places greater demands on our ability to accurately predict and control the steady and unsteady hydrodynamic loads on submerged structures at high Reynolds number. The particular application that stimulated the present study relates to the construction of piers for a long-span bridge in a deep, fast-moving river. In such projects, large, steel-walled caissons are lowered in place to provide dry space for the construction of the piers (Krishna et al. 2004). The caissons' cross-sectional geometries are invariably bluff leading to massive flow separation and large drag forces. Moreover, the flow separation is often unsteady due to the occurrence of vortex shedding leading to substantial fluctuations in both the lift and drag forces that occur at a well-defined (Strouhal) frequency. Since the caissons are by their nature temporary structures, they are often constructed in several sections from thin steel plates whose thickness is determined by estimates of the lift and drag forces they are likely to experience once fully submerged. The occurrence of vortex shedding demands further consideration to guard against failure by resonance or fatigue. The ability to accurately predict the magnitude and frequency of these forces on the full-scale caissons is clearly crucial for their safe and cost-effective construction. Experimental data that can guide the design are limited by the fact that the Reynolds numbers associated with the full-scale dimensions and the river-flow velocities by far exceed the

values of this parameter attained in laboratory studies. This can clearly be seen from Fig. 1 where many of the available experiments on cylinders having a rectangular cross section (which is the typical caisson cross-sectional geometry) are plotted. Discarding the experiments where the aspect ratio of $B$ (the dimension parallel to the flow) to $D$ (the dimension perpendicular to it) is less than unity on the basis that it would be unusual to orient the caisson in such a way as to maximize the drag, it is evident that the vast majority of measurements are for the case of a square cylinder ($B/D = 1$), with the measurements becoming more sparse at higher values of this ratio. For the particular full-scale caisson under present consideration, $B/D = 1.564$, and only one result for a similar ratio could be found (Shimada and Ishihara 2002). Even then, the result was the outcome of a computational rather than experimental study, and at a Reynolds number that is about two orders of magnitude lower than the value expected in the river deployment. Extrapolation of available measurements to higher Reynolds numbers is certainly possible, but considering the inevitable uncertainty in fluid-flow measurements and the indeterminate extent of the scaling effects that would be present, it seemed logical to seek to obtain the necessary data using computational fluid dynamics with the proviso that the results obtained are convincingly shown to be of demonstrable reliability to be of any value in the design of a full-scale caisson.

In addition to providing reliable estimates of the hydrodynamic loads on the caisson, another objective of this study was to assess the effectiveness of alternative techniques for reducing the magnitudes of both the mean and the fluctuating components of these loads. This is important in practice as it allows for the achievement of better control of the caisson sinking process (Yang et al. 2019, 2022). Attention here was confined to consideration of passive vortex shedding control methods that do not require the input of energy for their operation. Two techniques were considered. The first involved replacing the sharp corners by rounded ones. This simple adaptation to the cross-sectional geometry has been shown to produce an appreciable reduction in the lift and drag forces on square

[1]Professor, School of Highway, Chang'an Univ., Xi'an, Shaanxi 710064, China (corresponding author). Email: niuyanwei@chd.edu.cn

[2]Professor, Dept. of Civil & Environmental Engineering, Univ. of California, Davis, CA 95616. ORCID: https://orcid.org/0000-0002-3437-1219
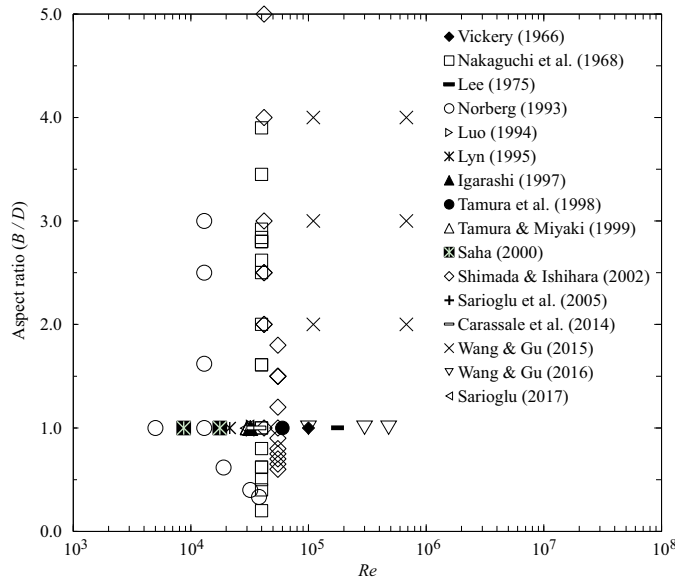
**Fig. 1.** Experiments on rectangular cylinders with sharp corners.

cylinders (Tamura et al. 1998; Miran and Sohn 2015; Carassale et al. 2014; Wang and Gu 2016; Dai et al. 2017) and on cylinders having aspect ratios different from unity. Thus, for example, Norberg (1993) experimentally investigated cylinders with aspect ratio in the range 1–3 while Wang and Gu (2015) experimentally investigated rectangular geometries with side ratios in the range 2–4. Their results will provide useful benchmarks for checking the present computations. Another passive technique with proven performance that is considered here involves the use of a splitter plate installed at the rear of the cross-sectional area (Dai et al. 2018). While rounding the corners and adding a splitter plate have proved to be quite effective when deployed separately, no previous work could be found to show their performance when deployed simultaneously. Moreover, the effectiveness of these techniques have been demonstrated for values of $Re$ below $2 \times 10^5$ while, in the present application, interest is in the flow behavior around a full-scale structure at values of Re of order $10^7$. This paper reports on computations performed for both techniques, and will present recommendations that were actually deployed in practice.

## Mathematical Formulation

### Governing Equations

The equations that govern the conservation of mass, momentum applicable to both the unsteady Reynolds-averaged Navier-Stokes (URANS) and the large-eddy simulations (LES) approaches are of the form

$$\frac{\partial \bar{U}_i}{\partial x_i} = 0 \tag{1}$$

$$\frac{\partial \bar{U}_i}{\partial t} + \frac{\partial}{\partial x_j}(\bar{U}_i \bar{U}_j) = -\frac{1}{\rho}\frac{\partial \bar{p}}{\partial x_i} + \frac{\partial}{\partial x_j}\left(\nu \frac{\partial \overline{U_i}}{\partial x_j}\right) + \frac{\partial \tau_{ij}}{\partial x_i} \tag{2}$$

where an overbar represents a time-averaged or a space-filtered quantity; and $\tau_{ij}$ are unknown turbulence correlations that arise from the averaging process.

For URANS, $\tau_{ij}$ are the Reynolds stresses, which, for the eddy-viscosity turbulence models used in the present study, are obtained from Boussinesq's linear stress-strain relationship

$$\tau_{ij} = 2\nu_t S_{ij} - \frac{2}{3}\delta_{ij}k \tag{3}$$

where $S_{ij}$ = mean rate of strain

$$S_{ij} = \frac{1}{2}\left(\frac{\partial U_i}{\partial x_j} + \frac{\partial U_j}{\partial x_i}\right) \tag{4}$$

and $\nu_t$ = turbulent kinematic viscosity:

$$\nu_t = C_\mu \frac{k^2}{\epsilon} \tag{5}$$

In the previous equations, $k$ and $\epsilon$ are, respectively, the turbulence kinetic energy and its dissipation rate, which are obtained from the equations

$$\frac{\partial k}{\partial t} + U_j \frac{\partial k}{\partial x_j} = \frac{\partial}{\partial x_j}\left[\left(\nu + \frac{\nu_t}{\sigma_k}\right)\frac{\partial k}{\partial x_j}\right] + P_k - \epsilon \tag{6}$$

$$\frac{\partial \epsilon}{\partial t} + U_j \frac{\partial \epsilon}{\partial x_j} = \frac{\partial}{\partial x_j}\left[\left(\nu + \frac{\nu_t}{\sigma_\epsilon}\right)\frac{\partial \epsilon}{\partial x_j}\right] + C_{\epsilon 1}\frac{\epsilon}{k}P_k - C_{\epsilon 2}\frac{\epsilon^2}{k} - R \tag{7}$$

where $P_k$ = rate of production of turbulence kinetic energy

$$P_k = 2\nu_t S_{ij} S_{ij} \tag{8}$$

One of the turbulence models used in this work is a variant on the standard $k$-$\epsilon$ model and is referred to hereafter as the *modified* model. It was specifically developed in order to account for the effects of the interactions between organized mean-flow unsteadiness (vortex shedding in this case) and the random turbulent motions (Younis and Przulj 2006). These interactions lead to a direct input of energy into the turbulent-energy spectrum at a discrete frequency—the Strouhal frequency. The modification entails making the coefficient $C_{\epsilon 1}$ dependent on the rate of additional energy input. This is achieved simply by multiplying this coefficient by the quantity $T$, which is defined as

$$T = \left(1 + C_t \frac{k}{\epsilon}\frac{1}{Q+k}\left|\frac{\partial(Q+k)}{\partial t}\right|\right) \tag{9}$$

where $Q$ = mean-flow kinetic energy. The values assigned to the model coefficients are given in Table 1.

The second model considered is the widely-used *RNG* model (Yakhot and Orszag 1986; Yakhot et al. 1992), which has given improvements over the standard model in a number of applications. The model introduces an additional term $R$ to the $\epsilon$ equation having the form

$$R = \frac{C_\mu \eta^3 (1 - \eta/\eta_0)}{1 + \beta \eta^3}\frac{\epsilon^2}{k} \tag{10}$$

**Table 1.** Turbulence models coefficients

| $k$-$\epsilon$ model | $C_\mu$ | $C_{\epsilon 1}$ | $C_{\epsilon 2}$ | $C_t$ | $\sigma_k$ | $\sigma_\epsilon$ | R |
|---|---|---|---|---|---|---|---|
| Standard | 0.09 | 1.44 | 1.92 | 0 | 1.0 | 1.3 | 0 |
| Modified | 0.09 | 1.44$T$ | 1.92 | 0.38 | 1.0 | 1.3 | 0 |
| RNG | 0.0845 | 1.42 | 1.68 | 0 | 0.718 | 0.718 | Eq. (10) |

where $\beta = 0.012$; and $\eta_0 = 4.38$. The values of the remaining coefficients are listed in Table 1.

For the large-eddy simulations, $\tau_{ij}$ are the subgrid scale stresses, which are modeled following Smagorinsky (1963) as

$$\tau_{ij} = -\nu_{sgs} 2\bar{S}_{ij} \tag{11}$$

where $\bar{S}_{ij}$ = resolved strain rate tensor as defined previously; and $\nu_{sgs}$ = subgrid scale eddy viscosity, which is obtained from

$$\nu_{sgs} = (C_S \Delta)^2 |\bar{\mathbf{S}}| \tag{12}$$

where $C_S$ was set equal to 0.20; and $\Delta$ = representative length scale obtained from

$$\Delta = (\Delta_x \Delta_y \Delta_z)^{\frac{1}{3}} \tag{13}$$

where $\Delta_x, \Delta_y$, and $\Delta_z$ are the grid node spacing in the $x$, $y$, and $z$ directions, respectively.

Following the usual practice, we use van Driest's damping function to bring about the correct behavior

$$\nu_{sgs} = (C_S \Delta)^2 |\bar{\mathbf{S}}|(1 - e^{-y^+/A^+}) \tag{14}$$

where $y^+ = (u_\tau y/\nu)$ = nondimensional wall distance; and $A^+ = 26$.

### Computational Details

The governing equations were solved by finite volume methodology incorporated in OpenFOAM version 5.0. The Laplacian terms were discretized using the Gauss linear corrected scheme, while the convective fluxes were approximated using the Gauss limited linear V integral discrete lattice. The temporal terms were discretized by using the Euler scheme. The PISO algorithm (Issa 1986) was used to couple the solution of the continuity and momentum equations. The convergence criterion for the iterative solution procedure at each time step was set to be when the normalized residuals fell below $10^{-6}$. The time step size was restricted according to the Courant-Friedrichs-Lewy number

$$CFL = \Delta t \max\left(\frac{|U|}{\Delta x} + \frac{|V|}{\Delta y} + \frac{|W|}{\Delta z}\right) \tag{15}$$

To ensure stability, $CFL$ was set equal to 0.6 for $Re$ up to $3 \times 10^5$ and 1.0 for $Re$ up to $10^7$ to ensure time accurate and stable results.

A multiblock solution methodology was adopted for in which the computational domain was subdivided into a number of blocks in order to facilitate parallel computations on distributed processors (Fig. 2). The boundary conditions employed were as follows. At the inlet, uniform profiles of the streamwise velocity $U_0$ were set according to the required Reynolds number. The specification of a uniform profile instead of a boundary-layer one was justified in this study where the focus was on an isolated segment of the caisson rather than on the complete structure. The value of $k$ was then obtained from $k = (3/2)(T_u U_0)^2$ where $T_u$ is the inlet turbulence intensity, which was set here to 0.5%, which is representative of the levels found in wind-tunnel studies (Tamura et al. 1998; Wang and Gu 2015; Luo et al. 1994; Sarioglu et al. 2005). The dissipation rate $\epsilon$ is typically obtained by inversion of the relation for the eddy viscosity $\nu_t$ [Eq. (5)]. Alternatively, a constant ratio $\nu_t/\nu$ is specified and $\epsilon$ is then deduced from that value (Dai et al. 2018; Jones et al. 2016). In this study, consideration was given to using a Reynolds number–dependent approach to specifying $\nu_t/\nu$. Younis and Przulj (2006) proposed an equation that took into account the ratio of the integral length scale of turbulence to the physical dimensions of the cylinder. For the present conditions, this yielded

$$(\nu_t/\nu)_0 \approx 0.22 T_u Re \tag{16}$$

This approach was tested and the results are described in the next section.

At outlet to the solution domain, the streamwise gradients of all the dependent variables were set equal to zero. Similarly, the normal gradients were set equal to zero at the side planes. The cylinder walls were assumed to be smooth, and the flow in their immediate vicinity was assumed to follow the standard logarithmic law

$$\frac{U_p}{U_{\tau p}} = \frac{1}{\kappa} \ln\left(\frac{U_{\tau p} n_i}{\nu}\right) + E \tag{17}$$
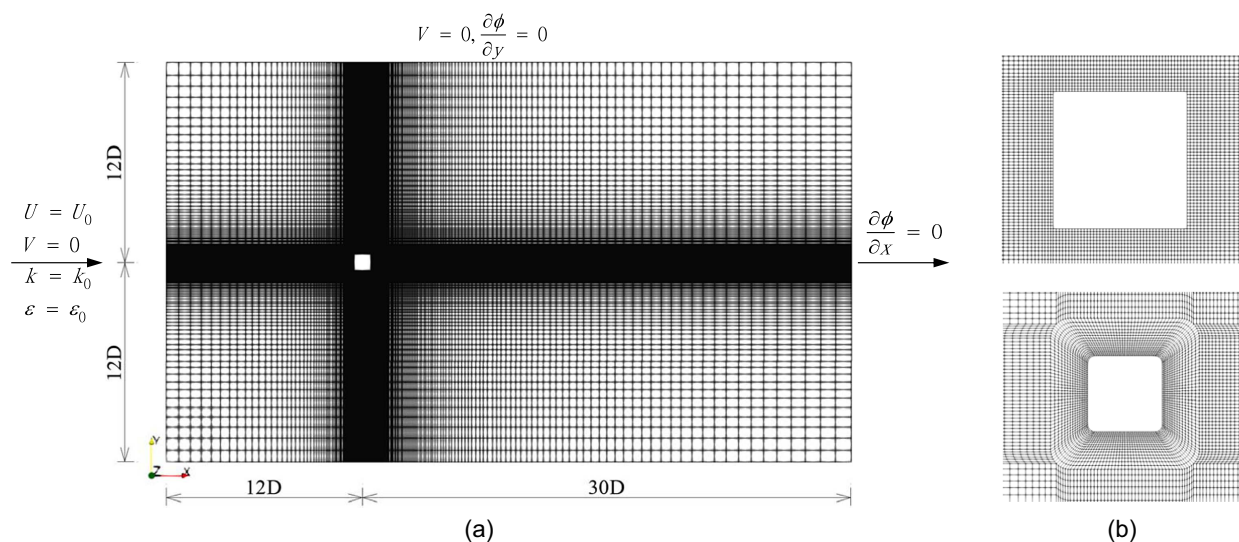


**Fig. 2.** Grid arrangement, boundary conditions, and monitoring section of square cylinder: (a) computational domain and grid distribution; and (b) mesh details near the square cylinder with rounded corner.

where $U_p$ = velocity component parallel to the wall; $U_{\tau p}$ = friction velocity; $\nu$ = kinematic viscosity; and $n_i$ = normal distance from the wall to the grid nodes closest to it. The coefficients $\kappa$ and $E$ were set equal to their standard values of 0.41 and 9.8, respectively (Schlichting and Gersten 2017). The boundary conditions for $k$ and $\epsilon$ at the cylinder wall were fixed by the assumption of local equilibrium.

## Results for Benchmark Flows

In this section, results obtained with the various models for a number of standard benchmark flows are presented. These flows were selected on the basis that they share many features of the flows around full-scale caissons.

### Square and Rectangular Cylinders

The dimensions of the computational domain, together with the boundary conditions are shown in Fig. 2. The dimension $D$ was set equal to 0.05 m. These dimensions were found to be appropriate to eliminate the influence of the boundary conditions and the blockage on the computations (Younis and Przulj 2006). The center of the square cylinder was located at $x = 12D$ and $y = 12D$, and the resulting blockage ratio was 4.1%. The computational model consisted of 31,749 cells using orthogonal mesh, with 43 cells in contact with each side of cylinder wall. The rectangular cross sections were generated by stretching the sides parallel to the flow. The number of cells in contact with the sides was adjusted to maintain the cell adjacent to the cylinder wall within a side ratio smaller than 5. Five aspect ratios $B/D$ were investigated, viz. 1.564 (which is the same ratio as that of the full-scale caisson), 2, 3, 4, and 5.

Experimental data available for model validation are available in the range $10^4 < Re < 10^5$. These included the measurements of Tamura et al. (1998) for $Re = 6 \times 10^4$, Carassale et al. (2014) for $Re = 3.6 - 3.7 \times 10^4$, Norberg (1993) for $Re = 0.5 - 3.8 \times 10^4$, Rathakrishnan (1999) for $Re = 5.8 - 9.5 \times 10^4$, and Vickery (1966) for $Re = 10^5$. Fig. 3 presents the time series of the hydrodynamic coefficients predicted by the various models for the case of flow around a square cylinder. The computations for the standard k-$\epsilon$ model were started from the prescribed inlet conditions. Each subsequent model calculations were started from the end of the preceding model in order to better illustrate the differences between their behavior. This practice, as opposed to the alternative of restarting each model from the original uniform flow field, was justified by the fact that the flow was periodic in nature and, as can be seen from Fig. 3, readjusted very rapidly to the change in model. The parameters plotted in this figure consist of the lift

coefficient ($C_L$), the drag coefficient ($C_D$), and the nondimensional time ($t^*$)

$$C_L = F_L \left/ \frac{1}{2}\rho U_0^2 D^2 \right. \tag{18}$$

$$C_D = F_D \left/ \frac{1}{2}\rho U_0^2 D^2 \right. \tag{19}$$

$$t^* = tU_0/L \tag{20}$$

where $F_L$ and $F_D$ are the combined pressure and viscous lift and drag forces, respectively. The pressure forces were obtained by integrating the computed static pressure on the caisson surface over the entire area and by resolving the resultant forces into their components. The viscous forces were obtained from the computed values of the wall shear stresses and the cell areas on which they apply, similarly resolved into their components. The time interval over which each model was used was the same and was equal to 480 in nondimensional time $t^*$. In this interval, 2,000 data points were generated; a number which is sufficient to compute the mean and RMS values of the force coefficients.

It is immediately evident that the standard k-$\epsilon$ model yields the lowest level of mean drag while predicting virtually no fluctuations in the lift coefficient. Both of these outcomes represent well-known defects in this model. The remaining models yield approximately the same level of fluctuations in $C_L$ while the RNG model fails to reproduce the level of fluctuations in $C_D$ obtained by the modified k-$\epsilon$ model and the LES.

Figs. 4(a and b) show the predicted contours of the instantaneous vorticity and the streamlines at the phase of shedding cycle, which corresponds to the point where the lift coefficient is at maximum. Plotted there is the nondimensional vorticity $v^* (= vD/U_0$, where $v$ is the vorticity component normal to the solution domain). It is apparent from these plots that a clearly defined vortex shedding process is captured by the modified k-$\epsilon$ model, which succeeds in capturing the experimentally-observed separation and subsequent reattachment that occurs along the cylinder's length.

Fig. 5 shows the predicted time-averaged pressure coefficient ($C_p = p/(1/2)\rho U_0^2$, $p$ is time-averaged pressure) and the mean streamwise velocity along the centerline. Also plotted there are experimental data from various sources (Lee 1975; Bearman and Obasaju 1982; Durao et al. 1998; Lyn 1992). The predicted size of the recirculation zone downstream of the square cylinder generally agrees well with the available experimental data.

An overall impression of the effects of the cylinder aspect ratio $B/D$ on the resulting flow patterns can be seen in Fig. 6, where results are presented for values of $B/D$ in the range 1–5. The plots
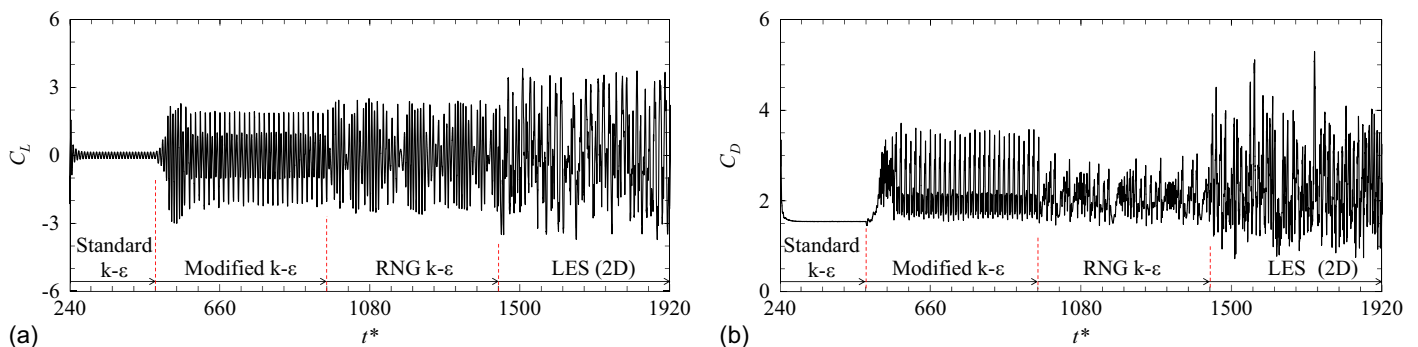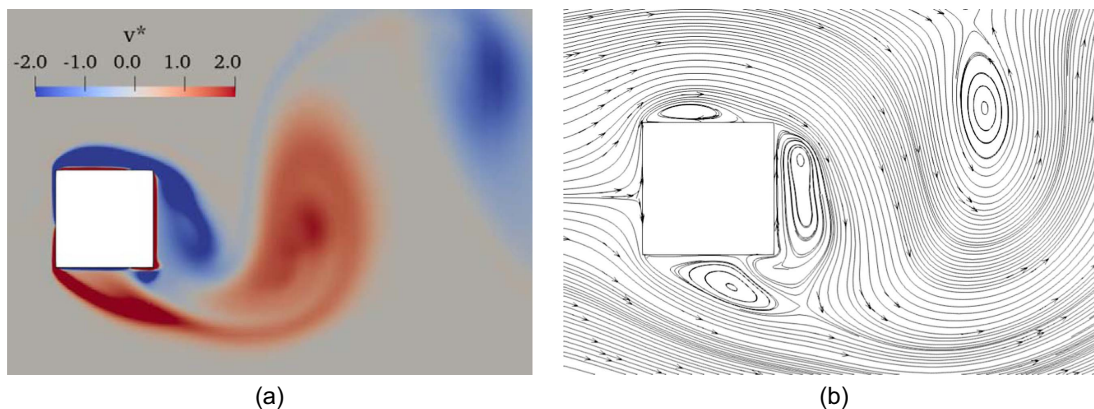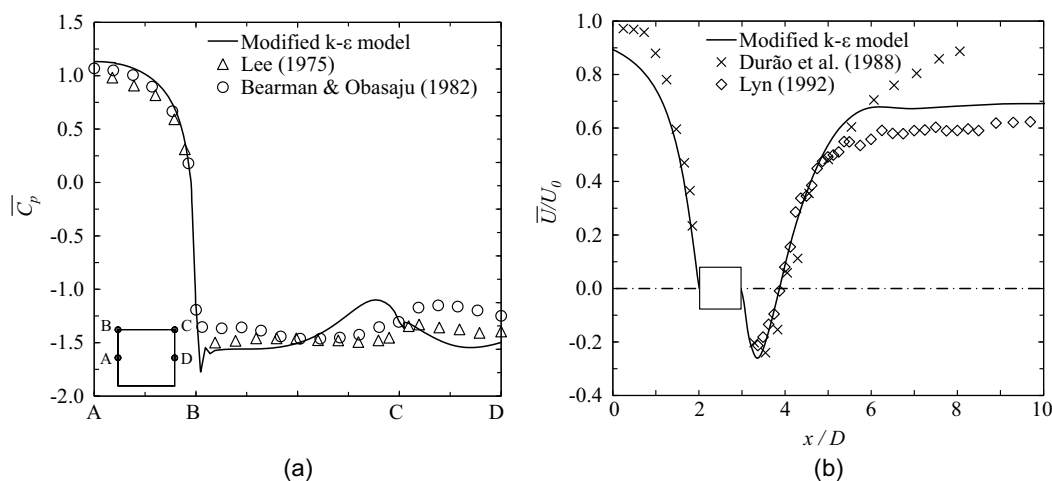


**Fig. 3.** Variation of the lift and drag coefficients with time for square cylinder at $Re = 6 \times 10^4$: (a) $C_L$; and (b) $C_D$.

**Fig. 4.** Contours of vorticity and streamlines at maximum $C_L$ for square cylinder at Re $= 6 \times 10^4$: (a) nondimensional vorticity; and (b) streamlines.



**Fig. 5.** Predicted and measured time-averaged pressure coefficient and centerline velocity for square cylinder at Re $= 6 \times 10^4$: (a) mean surface pressure coefficient; and (b) mean velocity along the centerline.

reveal complex patterns of flow separation and subsequent reattachment, and of separated wakes that are vastly different in size, indicating a strong dependence of the hydrodynamic forces on the aspect ratio. This is clearly evident from Fig. 7, where the average drag coefficient $C_D$ and the fluctuating component of the lift coefficient $C'_L$ are plotted. Generally, good correspondence is obtained between the models predictions and the experimental and LES results for $C_D$ across the entire range of $B/D$.

### Square Cylinder with Rounded Corners

Computations were performed for four ratios of the radius of the rounded corner ($r$) to the width ($D$) namely $r/D = 1/15$, $1/10$, $1/7.5$ and $1/6$. A qualitative description of the effects of $r/D$ on the overall flow patterns can be seen in Fig. 8.
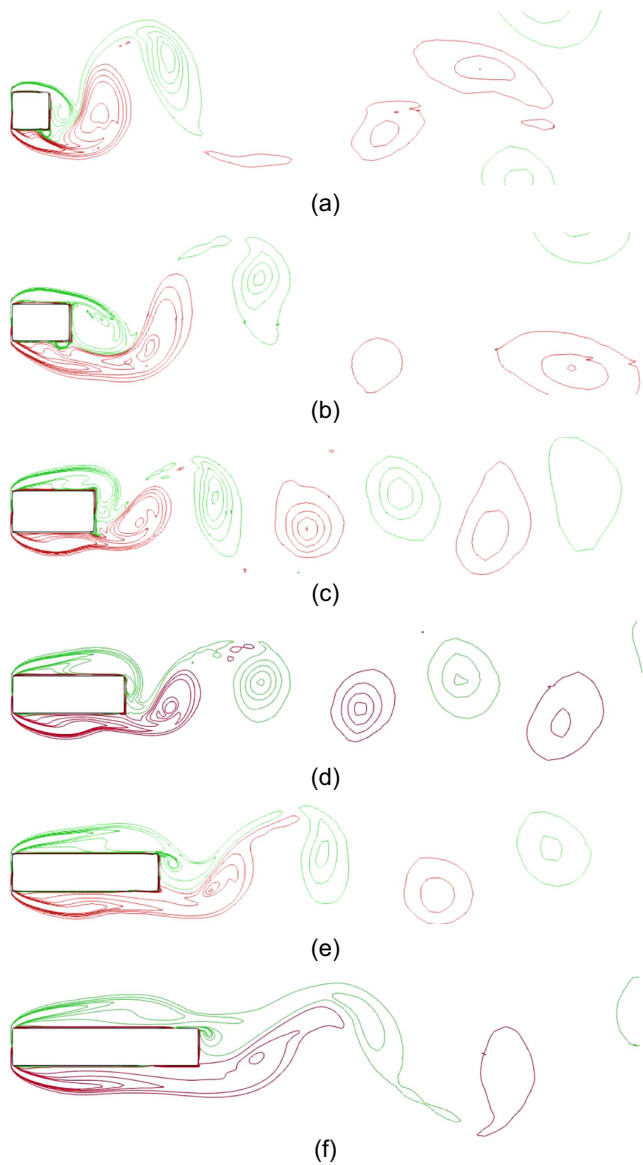
The predicted and measured variation of the mean drag and the fluctuating lift coefficients with $r/D$ is shown in Fig. 9 for the case where the turbulence intensity $T_u$ was 0.2%. As expected, the effects of rounding the sharp corners lead to marked decrease in $\overline{C_D}$ with an increase in $r/D$, which is indicative of the large changes in flow behavior brought about by the smooth transition over the cylinder and into the wake region. From a practical standpoint, the increase of $r/D$ means a significant reduction of the usable area

within the caisson and this places an upper limit on the value of $r/D$.

### Square Cylinder with Splitter Plate

The models' performance is next evaluated for the case of a square cylinder with a splitter plate placed at the mid-plan of the rearward side. Ten cases were considered, corresponding to ratios of the splitter plate length ($L$) to cylinder width $B$ of $L/B = 1/20$, $1/15$, $1/10$, $1/5$, ¼, $1/3$, $2/5$, ½, ¾, and 1.

The predicted and measured variation of the drag coefficient (normalized by its value for the case of no splitter plate) are shown in Fig. 10. The effect of the splitter plate on the drag coefficient is most pronounced for all values of $L/B$, with the rate of decrease being at its steepest for values of $L/B$ in the range 1/20–1/10. The reduction in $\overline{C_D}$ persists for higher values of $L/B$, albeit at a somewhat reduced rate. Similar trends are exhibited in both the predictions and the measurements, though some quantitative differences are apparent. Thus, for the case of $L/B = 1$, for example, the measurements of Rathakrishnan (1999) suggest that $\overline{C_D}$ has decreased by about 30% of its initial value, while the measurements of Sarioglu (2017) suggest a reduction of 22%. The modified $k - \epsilon$ model obtains a 20% reduction in this parameter.

**Fig. 6.** Predicted instantaneous spanwise vorticity contours around rectangular cylinders with various $B/D$ at the phase of maximum $C_L$ ($Re = 6 \times 10^4$). The anticlockwise rotation, $-4 < v^* < 4$: (a) $B/D = 1$; (b) $B/D = 1.564$; (c) $B/D = 2$; (d) $B/D = 3$; (e) $B/D = 4$; and (f) $B/D = 5$.
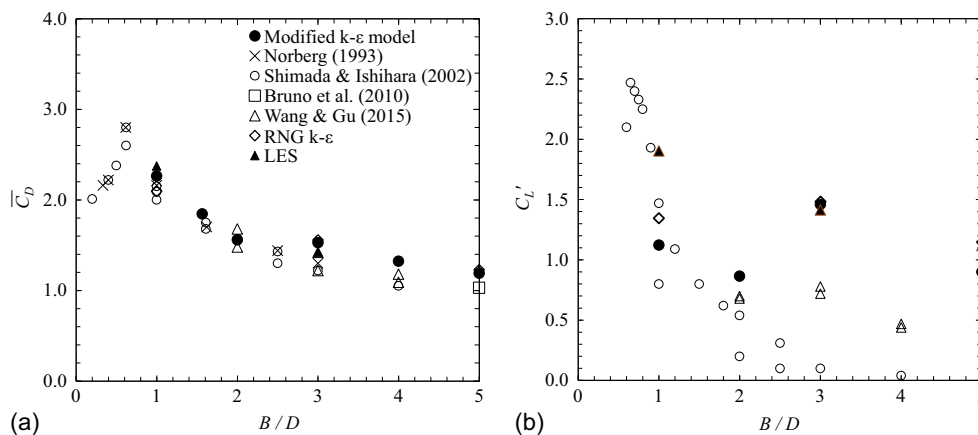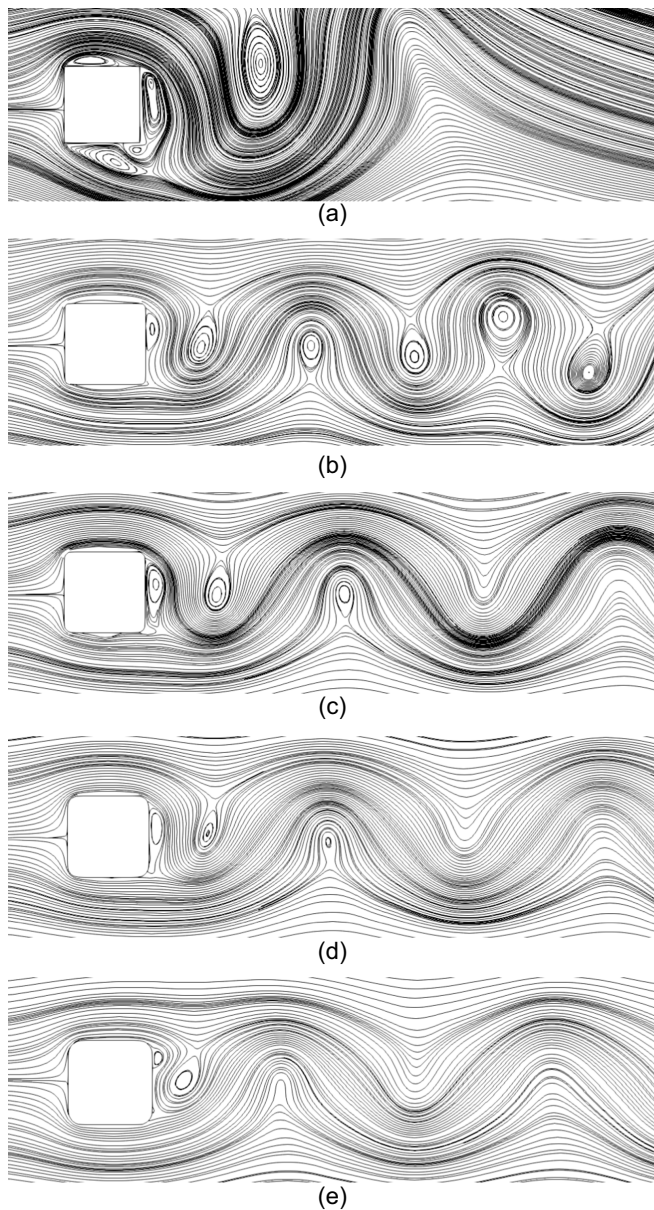
The predicted contours of mean vorticity for various values of $L/B$ are presented in Fig. 11. These contours were obtained at the phase in the vortex shedding cycle that corresponds to where the lift is at its maximum. It is generally assumed that the effectiveness of the splitter plates in reducing the drag is associated with their modification of the base flow by reducing the extent of the separated wake. This is clearly evident from this figure, especially at higher values of $L/B$ where the size of the shed vortices are markedly small leading to reduction in the force fluctuations as well. It should be noted that the splitter plates themselves may be subject to vibrations leading to fatigue damage and to alteration of the surrounding flow field. However, the extent of the latter is not thought to be sufficient to warrant a fully-coupled fluid-structures interactions (FSI) approach to this problem.
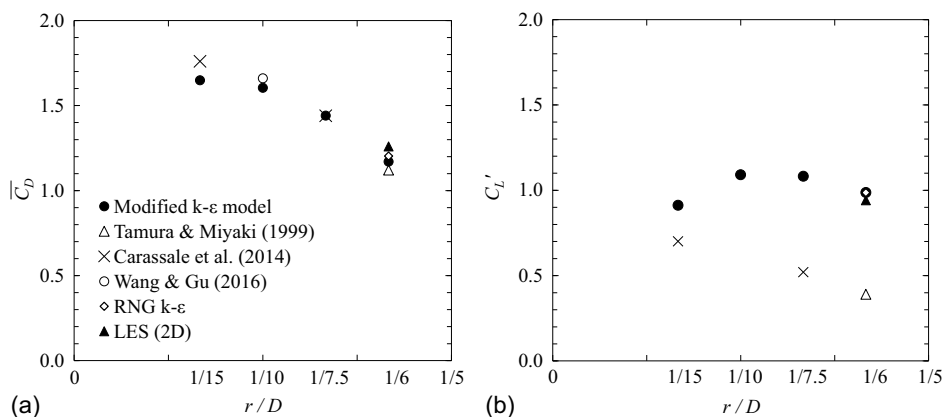
### Reynolds Number Effects

The models' ability to account for the effects of Reynolds number is assessed by computations performed for 10 different values in the range $0.5 \times 10^4 < Re < 9.4 \times 10^6$, with the highest value being appropriate for the operation of the full-scale caisson of present interest.

The predicted and measured variation of the hydrodynamic parameters with $Re$ for the case of a square cylinder is shown in Fig. 12. Also plotted there are the LES results of Sohankar (2006). Although the experimental results show a certain degree of scatter, the data for $\overline{C_D}$ fall in the range of 2.03–2.30. The variations among the experiments are largely due to the different levels of turbulence intensity in the experiments. Thus, for example, there are three points (marked by hollow triangles) in Fig. 12 at $Re = 3 \times 10^4$ suggesting a $\overline{C_D}$ value of 2.1 for $T_u = 0.4\%$, but this reduces to 1.5 at the higher $T_u$ value of 14%. Similarly, the levels obtained in the experiments of Vickery (1966) and Lee (1975) were lower at $T_u$ of 10% and 12.5%, respectively. In contrast, the lower values of $T_u$ in the experiments by Igarashi (1997) (0.4%) and Sarioglu (2017) (0.8%), yielded higher values of $\overline{C_D}$. Based on experimental and computation results, Bai and Alam (2018) argued that $\overline{C_D}$ approached a constant level at values of $Re$ greater than $10^4$ and a value of 2.21 was suggested. Interestingly, the phenomenon of drag crisis does not seem to occur as it does for the case of a circular cylinder at high Re. It should be noted that based on experimental results of Wang and Gu (2016) and the LES results of Sohankar (2006), $\overline{C_D}$ is slightly higher and falls into range of 2.2 to 2.4. The Reynolds number of simulation in present study extends to $9.4 \times 10^4$. It can be seen that the modified k-$\epsilon$ model shows an



**Fig. 7.** Predicted and measured variations of $\overline{C_D}$ and the fluctuating lift coefficient $C'_L$ with $B/D$ ($Re = 6 \times 10^4$): (a) $\overline{C_D}$; and (b) $C'_L$.

**Fig. 8.** Streamlines of flow over square cylinders with different rounded corner ratio ($Re = 6 \times 10^4$): (a) sharp corner; (b) $r/D = 1/15$; (c) $r/D = 1/10$; (d) $r/D = 1/7.5$; and (e) $r/D = 1/6$.

increase in $\overline{C_D}$ from 1.95 to 2.23 as a result of an increase in $Re$ from $5 \times 10^3$ to $2 \times 10^4$. The Reynolds number effect on $St$ is shown in Fig. 12(b) where it can be seen that the predictions obtained by the variants of the k-$\epsilon$ model provide a good representation of the measurements.

Next, the effects of $Re$ on the average drag coefficient of a rectangular cross section having $B/D$ ratio of 1, 1.564 (which equals the ratio for the full-scale caisson), and 2 are explored. The results are shown in Fig. 13. It is seen that $\overline{C_D}$ remains fairly constant at value of $Re > 2 \times 10^4$. At $Re$ around $10^5$, the present simulations for the $B/D = 2$ case are in good agreement with the consensus of the experimental data. The computed $\overline{C_D}$ for the $B/D = 1.564$ case fall in between the data of Norberg (1993) and Nakaguchi et al. (1968).

## Results for the Full-Scale Caisson

This section presents the results of simulations performed on the full-scale caisson in the field operating conditions.
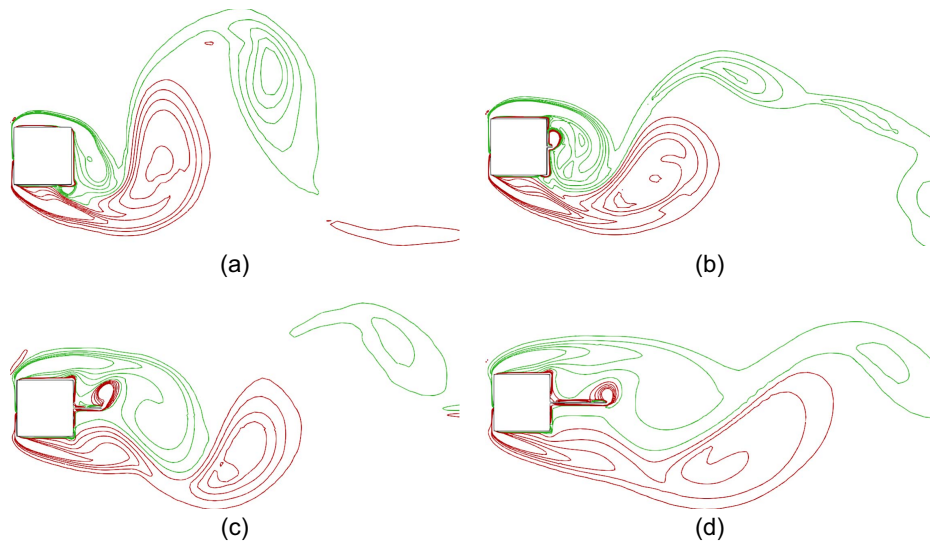
### Caisson Geometry and Computational Details

A schematic representation of the caisson is shown in Fig. 14(a). The cross-sectional dimensions are $29.4m \times 18.8m$ ($B/D = 1.564$).
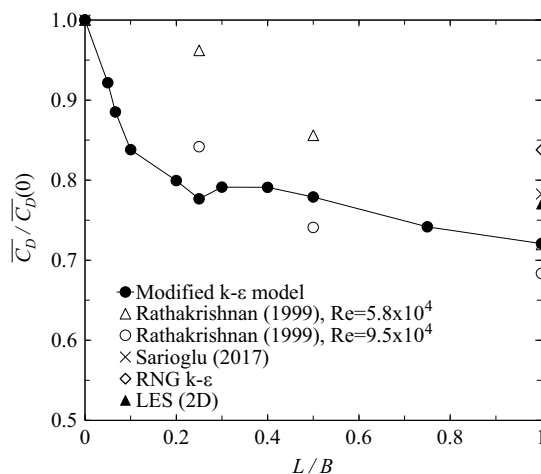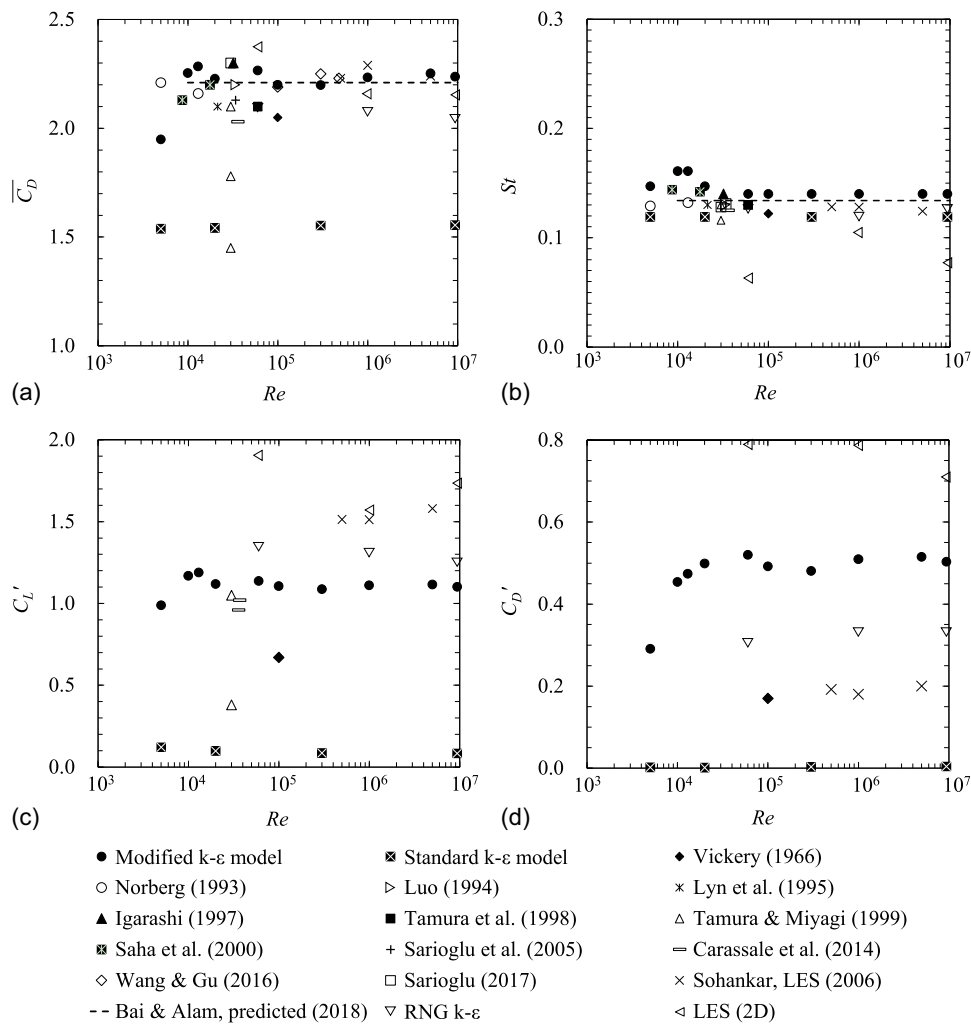


**Fig. 10.** Variation of average drag coefficient with $L/B$ ($Re = 6 \times 10^4$).



**Fig. 9.** Predicted and measured variation of hydrodynamic forces with $r/D$ for $Re = 6 \times 10^4$ and $T_u = 0.2\%$: (a) $\overline{C_D}$; and (b) $C_L'$.

**Fig. 11.** Predicted instantaneous spanwise vorticity contours around square cylinders with various $L/B$ at the phase of maximum $C_L$ ($Re = 6 \times 10^4$). Anticlockwise rotation, $-4 < v^* < 4$: (a) no splitter plate; (b) $L/B = 1/10$; (c) $L/B = 1/2$; and (d) $L/B = 1$.



Legend:
- ● Modified k-ε model
- ⊠ Standard k-ε model
- ◆ Vickery (1966)
- ○ Norberg (1993)
- ▷ Luo (1994)
- ✶ Lyn et al. (1995)
- ▲ Igarashi (1997)
- ■ Tamura et al. (1998)
- △ Tamura & Miyagi (1999)
- ⊠ Saha et al. (2000)
- + Sarioglu et al. (2005)
- ═ Carassale et al. (2014)
- ◇ Wang & Gu (2016)
- □ Sarioglu (2017)
- × Sohankar, LES (2006)
- ‐‐ Bai & Alam, predicted (2018)
- ▽ RNG k-ε
- ◁ LES (2D)

**Fig. 12.** Reynolds number effects on the computed and measured hydrodynamic parameters of square cylinder: (a) $\overline{C_D}$; (b) $St$; (c) $C_L'$; and (d) $C_D'$.
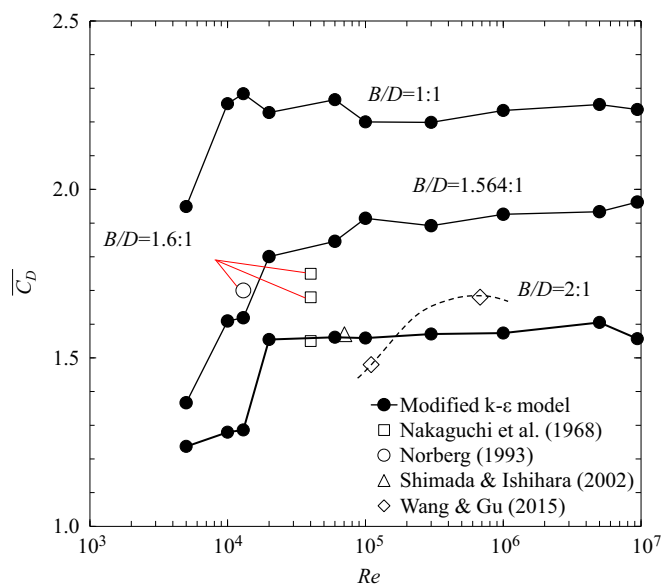
**Fig. 13.** Reynolds number effect on mean drag coefficient $\overline{C_D}$ for various values of $B/D$.

These dimensions provide a dry construction space beneath the water level for the pile cap having a rectangular section of dimensions 25.2 m × 14.6 m and an access margin of 0.5 m. The maximum flow velocity that was expected to occur during construction was 0.5 m/s. The resulting Reynolds number is Re = $9.4 \times 10^6$. The steel caisson was composed of seven segments, each 6 m in length. Fig. 14(b) shows the geometry adaptations to the original sharp-cornered rectangular cross section that were considered. These consisted of rounding the corners and attaching splitter plates to both the front and rear of the caisson either separately or simultaneously. All of the splitter plates were set along the caisson's centerline.

Because of the requirements of operation space and the bearing capacity, the limit radii (center at corners of pile cap) of the rounded corner considered was 2.1 m for the outer wall and 0.5 m for the inner wall. With these dimensions, an operating space was provided that was 0.5 m wide between the inner wall and pile cap, at a depth of 1.6 m of the full-scale caisson. Two configurations for the rounded corners were considered corresponding to the ratio of radius ($r$) to caisson width ($D$) of 1/15 and 1/8.95 (yielding radii of 1.253 m and 2.1 m, respectively). A total of 11 splitter plate lengths were computed in which the ratio of the splitter plate length to caisson length varied in the range $1/50 < L/B < 1$. This translated to actual splitter plate lengths in the range $0.588m < L < 29.4m$.

Three three-dimensional (3D) full-scale models were built in order to evaluate the hydrodynamic forces and to assess the effects of rounding the corners and attaching the splitter plates. Figs. 15(a–c) show a close-up of the mesh surrounding the caisson. All of the models use structured meshes including the transitional region, which is contiguous to the round corner. In the spanwise direction, 90 layers of cells were used to capture flow features in that direction.

To be able to quantify the numerical accuracy of the results, computations were performed on three different grids that consisted of 1,053,104, 1,373,988 and 1,780,800 nodes. A qualitative impression of the grid effects can be seen in Fig. 16 where the contours of nondimensional vorticity at maximum $C_L$ are shown. While the overall flow patterns obtained with each mesh are very similar, differences are observed in the smaller flow structures, especially those that develop close to the walls.

A quantitative check of the numerical accuracy of the computations was performed using the grid convergence index (GCI) method (Celik et al. 2008). The results of this check are presented in Table 2. In that table, the parameters that were chosen to test for
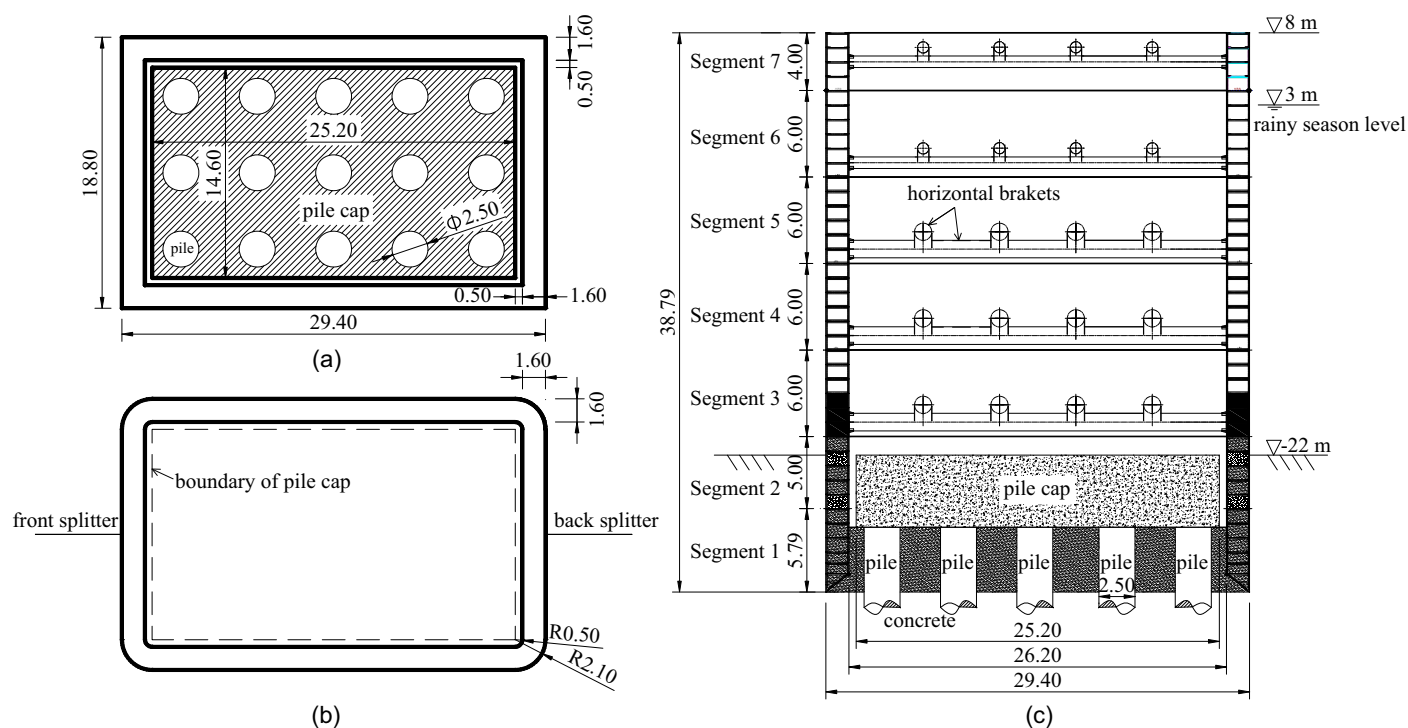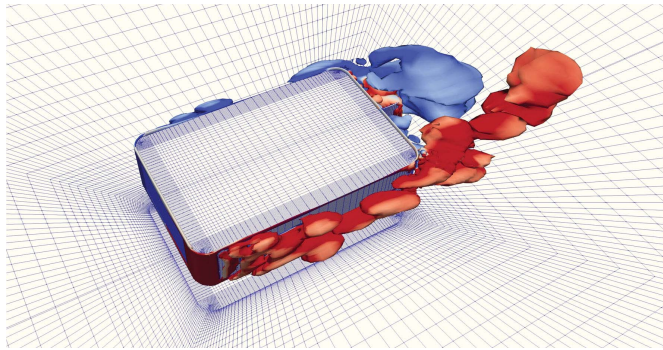


**Fig. 14.** Scale of actual steel caisson (all dimensions are in m): (a) cross section of steel caisson showing the multiple piles and the pile cap; (b) geometry adaptations considered; and (c) elevation of completed steel caisson and fabricated segments.
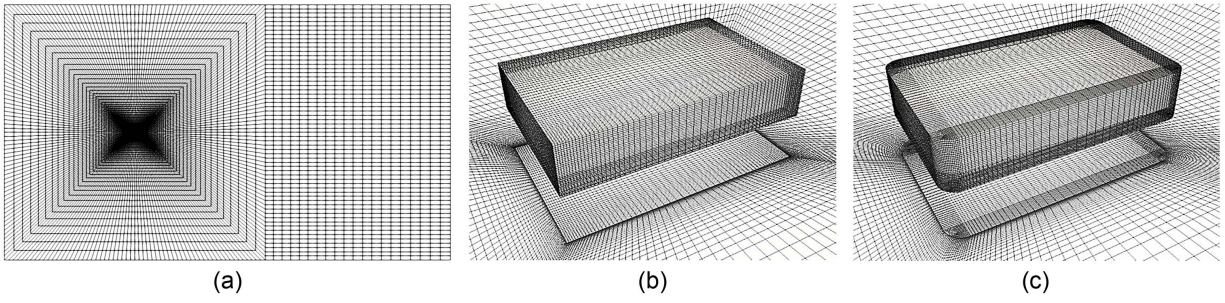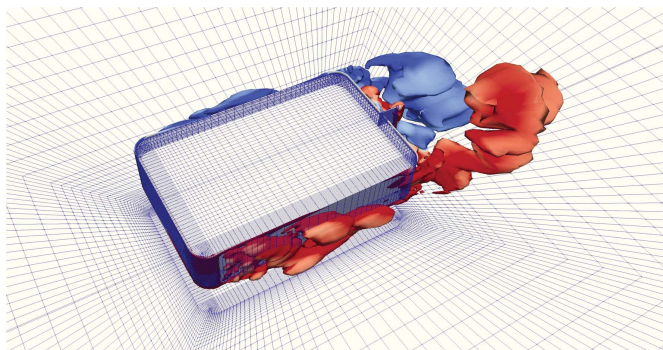
**Fig. 15.** 3D LES model: (a) plan view; (b) sharp corner details; and (c) round corner details.
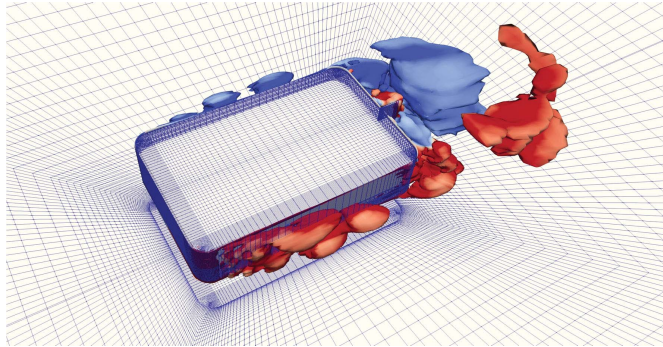


(a)



(b)



(c)

**Fig. 16.** Predicted instantaneous vorticity at maximum $C_L$ for full-scale caisson with rounded corners and splitter plate: (a) 1,780,800 nodes; (b) 1,373,988 nodes; and (c) 1,053,104 nodes.

grid independence are listed at the top and are labeled $N$. The symbol $\gamma$ represents the ratio of nodes in successive grids. The values listed under the label $\phi$ represent the values obtained for the chosen parameters with the selected grid. The values listed under the label

**Table 2.** The GCI method estimates of the discretization errors for the full-scale caisson computations at $Re = 9.4 \times 10^6$

| Variables/ coefficients | $\phi = \overline{C_D}$ | $\phi = S_t$ | $\phi = C_L'$ | $\phi = C_D'$ |
|---|---|---|---|---|
| $N_1, N_2, N_3$ | | 1,780, 800, 1,373, 988, 1,053, 104 | | |
| $\gamma_{21}$ | 1.296 | — | — | — |
| $\gamma_{32}$ | 1.305 | — | — | — |
| $\phi_1$ | 0.700 | 0.248 | 0.242 | 0.043 |
| $\phi_2$ | 0.698 | 0.239 | 0.258 | 0.035 |
| $\phi_3$ | 0.691 | 0.220 | 0.311 | 0.035 |
| $p$ | 6.310 | 2.673 | 4.569 | 14.183 |
| $\phi_{21}^{ext}$ | 0.700 | 0.257 | 0.235 | 0.044 |
| $e_{21}^r$ | 0.002 | 0.037 | 0.267 | 0.199 |
| $GCI_{21}$ | 0.001 | 0.046 | 0.037 | 0.006 |

**Table 3.** Computed drag coefficient and Strouhal number for models of different proportions

| Model scale | $B/D$ | $Re$ | $\overline{C_D}$ | $St$ | $C_L'$ | $C_D'$ |
|---|---|---|---|---|---|---|
| Small scale | 1.564 | $6.0 \times 10^4$ | 1.846 | 0.084 | 1.494 | 0.334 |
| ($D = 0.05$ m) | 2 | $6.0 \times 10^4$ | 1.561 | 0.196 | 0.867 | 0.080 |
| | 1.564 | $9.4 \times 10^6$ | 1.962 | 0.084 | 1.730 | 0.425 |
| Full scale | 1.564 | $6.0 \times 10^4$ | 1.854 | 0.084 | 1.479 | 0.336 |
| ($D = 18.8$ m) | 2 | $6.0 \times 10^4$ | 1.561 | 0.196 | 0.869 | 0.080 |
| | 1.564 | $9.4 \times 10^6$ | 2.006 | 0.091 | 1.781 | 0.455 |

$\phi_{21}^{ext}$ represent the asymptotic values for each of the target parameters, obtained by Richardson interpolation. Finally, the values listed under the label $e_{21}^r$ represent the resulting error. It is evident that the results obtained with the finest grid tested (1,780,800 nodes) are of sufficient numerical accuracy and hence all subsequent computations were performed using this grid.

### Basic Geometry

The results for the basic geometry with its sharp corners and with no splitter plate are presented first. The predicted hydrodynamic parameters obtained for two different values of $B/D$, and at two Reynolds number are shown in Table 3. The average drag coefficient $\overline{C_D}$ value of 2.006 obtained for the full-scale caisson is somewhat larger than the value of 1.962 obtained for a small-scale model having the same proportions. This may suggest that scaling effects that are present in experimental model tests are also present in the simulations, though the presence of any residual numerical artifacts in the latter can also have made a contribution to this result.
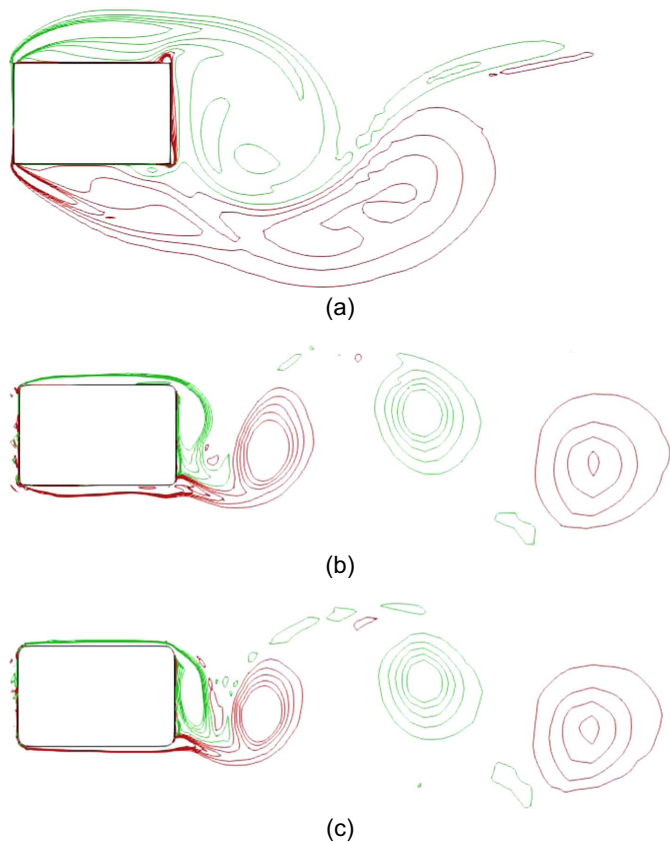
**Fig. 17.** Predicted instantaneous spanwise vorticity contours: (a) basic geometry of sharp corner; (b) $r/D = 1/15$; and (c) $r/D = 1/8.95$.

**Table 4.** Predicted hydrodynamic coefficients for full-scale caisson. Effects of rounding the corners

| $r/D$ | $Re$ | $\overline{C_D}$ | $St$ | $C_L'$ | $C_D'$ |
|---|---|---|---|---|---|
| 1/15 | $9.4 \times 10^6$ | 1.370 | 0.238 | 0.982 | 0.124 |
| 1/8.95 | $9.4 \times 10^6$ | 1.153 | 0.244 | 1.065 | 0.170 |
| 1/8.95 | $5.0 \times 10^6$ | 1.147 | 0.244 | 1.079 | 0.178 |

The mean vorticity is shown in Fig. 17(a) where it is clear that an extensive wake region develops downstream of the caisson leading to large mean drag and intense fluctuations in the lift and drag forces.
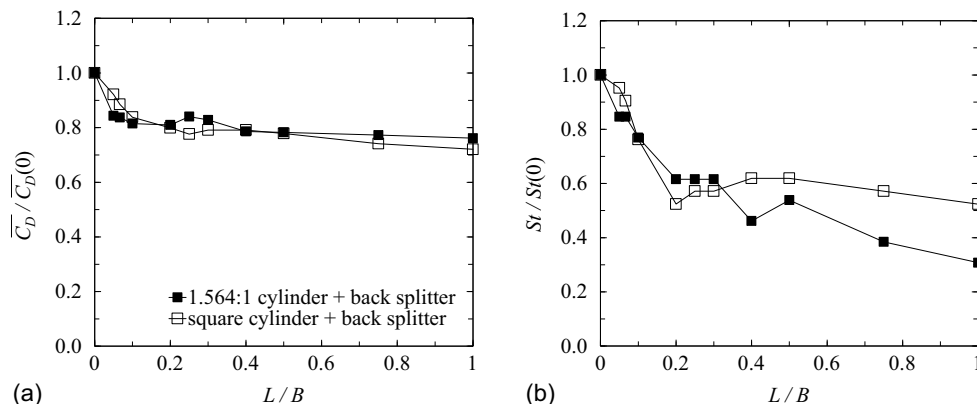
## Basic Geometry with Rounded Corners

The effects of rounding the corners on the flow patterns are shown in Figs. 17(b and c) for $r/D = 1/15$ and $1/8.95$, respectively. The most noticeable effects, compared to the case with the sharp corners, is the movement of the point of flow separation from the upstream corners to the downstream ones. This has the effect of significantly decreasing the size of the shed vortices and with that, the magnitude of the hydrodynamic forces on the caisson. This reduction of forces increases with $r/D$, as can be seen in Table 4. Thus, for example, compared to the sharp-cornered case, $\overline{C_D}$ is decreased by 31.7% with r = 1.253 m and 42.5% with r = 2.1 m. The Strouhal number is increased by the effects of rounding the corners consistent with the increase in the vortex shedding frequency in Fig. 17.
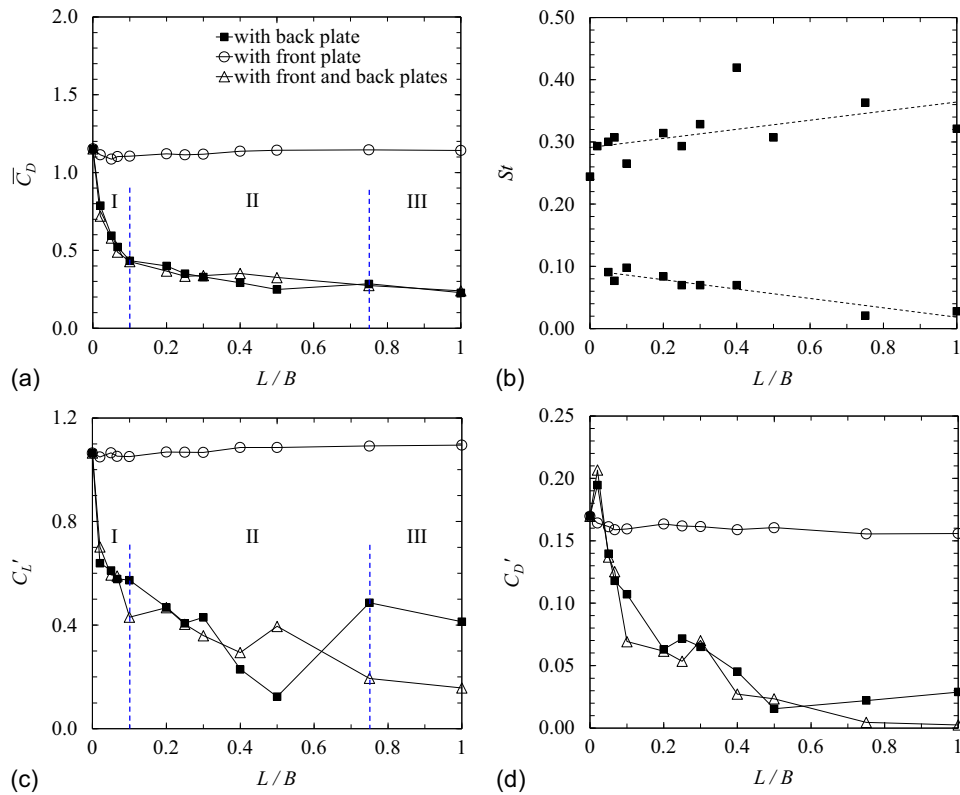
## Basic Geometry with Splitter Plates

The variation of the average drag coefficient and Strouhal number with the ratio $L/B$ is shown in Fig. 18. Plotted there are the computed results for the full-scale caisson and, for comparison, for a caisson having a square cross section. The results are normalized with respect to the values obtained for the basic geometry. For $L/B < 0.1$, the effects of the splitter plate are more pronounced for the 1.564 caisson.

## Basic Geometry with both Rounded Corners and Splitter Plate

Here, the corner radii were fixed at 2.1 m ($r/D = 1/8.95$) while the splitter plate was aligned with the caisson central line and placed either on the front, on the back, or on both the front and back simultaneously. When splitter plates were placed simultaneously at both the front and back, the plates were assumed to be of the same length. In total, 11 ratios of $L/B$ were considered, in the range from $1/50 < L/B < 1$. The results are shown in Fig. 19. It was found that the effect of placing the splitter plate on the front had very little effect on the hydrodynamic force and Strouhal number irrespective of the value of $L/B$. Consequently, this option was excluded from further consideration.

Based on the variation of $\overline{C_D}$ and $C_L'$ with $L/B$ for the case with the splitter plate at the back (Fig. 19), three distinct regimes can be identified:
- Regime I: $0 < L/B < 1/10$, $\overline{C_D}$ and $C_L'$ decrease rapidly;
- Regime II: $1/10 < L/B < 3/4$, moderate rate of decrease of $\overline{C_D}$;
- Regime III: $3/4 < L/B < 1$, $\overline{C_D}$ and $C_L'$ remain approximately constant.



**Fig. 18.** Variation of mean drag coefficient and Strouhal number with $L/B$: (a) $\overline{C_D}$; and (b) $St$.

**Fig. 19.** Computed hydrodynamic parameters for the case with rounded corners ($r/D = 1/8.95$) and splitter plates of various length: (a) $\overline{C_D}$; (b) $St$; (c) $C_L'$; and (d) $C_D'$.
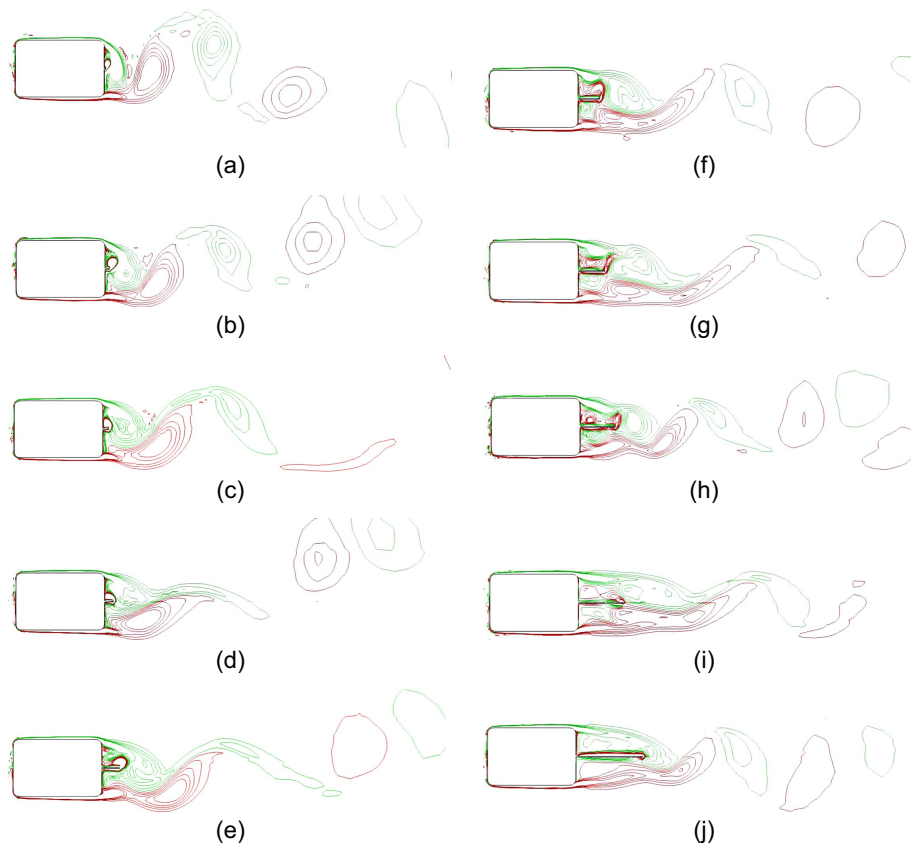


**Fig. 20.** Instantaneous spanwise vorticity contours at maximum $C_L'$. Results for the full-scale caisson with rounded corners modifying and for various values of $L/B$: (a) $1/50$; (b) $1/20$; (c) $1/15$; (d) $1/10$; (e) $1/5$; (f) $1/4$; (g) $1/3$; (h) $2/5$; (i) $1/2$; and (j) $3/4$.
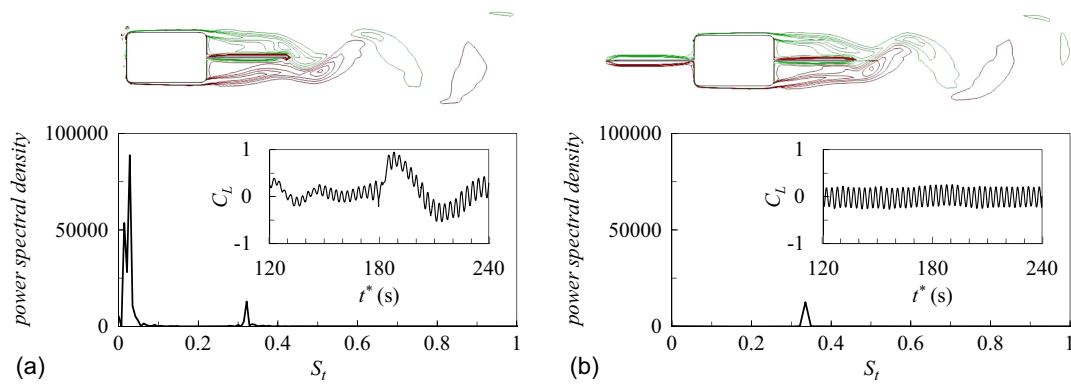
**Fig. 21.** Instantaneous vorticity, power spectral density, and time history of $C_L'$ for full-scale caisson with rounded corners and $L/B = 1$ at maximum $C_L$: (a) back plate; and (b) both front and back plates.
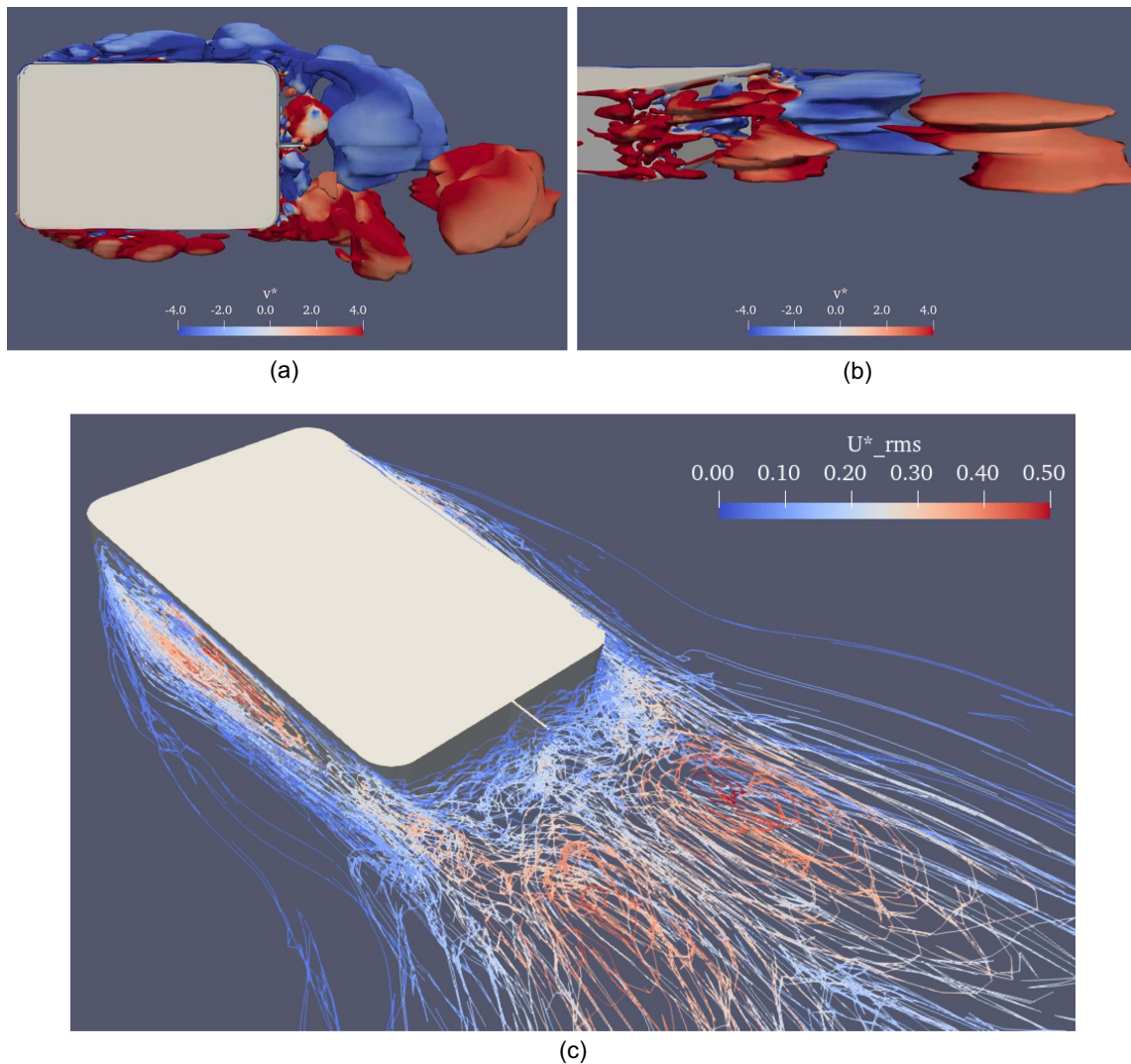


**Fig. 22.** Distribution of instantaneous vorticity ($v^*$) and fluctuating velocities for full-scale caisson with optimal rounded corners and splitter plate length. Contours of $v^*$, colored from $-4$ to $4$ and correspond to $0.001 < \lambda_2 < 6$: (a) plane view; (b) perspective view; and (c) perspective view of fluctuating velocities.

The mechanism of the transition of flow regimes can be seen from the variation of the flow characteristics in Fig. 20. The vorticity contours for this case obtained for various values of $L/B$ are shown in Fig. 20. For $L/B$ in the range $1/50 < L/B < 1/10$, small vortices are shed from the tip of the splitter plates, but because the splitter plates are short, the position of the main vortices are not altered and remain adjacent, close to the base face. The strength and size of the shed vortices are reduced leading to the reduction
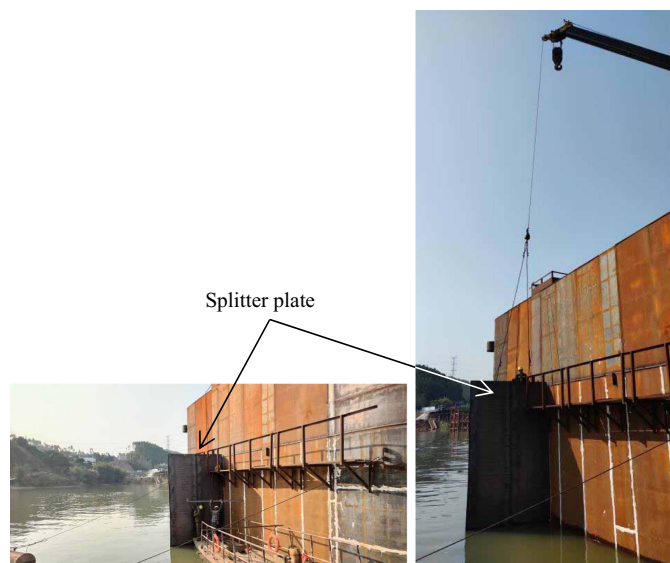
**Fig. 23.** Installation of splitter plate on the full-scale caisson. (Images by Yanwei Niu.)

of drag force. When $L/B$ is larger than $1/10$, the shed vortices are convected away from base leading to further reduction in drag.

When the length of the back splitter plate increases to $3/4B$, no significant change occurs in $\overline{C_D}$. However, $C_L'$ increases, although it is still less than that for the case with no splitter plate. The cause for this increase can be inferred from Fig. 21 where the time history for $C_L$ is shown, together with the fluctuations power spectral density. The fluctuations turn out to consist of a small amplitude high frequency component that is due to vortex shedding, and a low frequency large amplitude component due to the instability of the flow at the splitter plate tip. The addition of a splitter plate to the front side, as shown in Fig. 21(b), shows that the low frequency instability is effectively suppressed.

Figs. 22(a and b) present the flow structures that form when the optimal values of the corners radii and the splitter plate length are deployed. These plots are captured at the point of maximum $C_L$ and show the instantaneous normalized spanwise vorticity as detected using the $\lambda_2$ criterion (Jeong and Hussain 1995). The picture that emerges is of vortices that are somewhat diffused and intermingled compared to the case where no control methods were present. Fig. 22(c) depicts the contours of the root-mean-square of the fluctuations in the streamwise velocity, nondimensionalized by the inlet velocity. This parameter serves to quantify the strength and location of the formed vortices (Gerrard 1966). It can be seen that the most intense fluctuations occur at some distance downstream of the base.

Based on the results presented above, it was decided to implement both control methods in the full-scale caisson that was being deployed. In the first instance, the rounded corners were welded on the caisson segments as these were being fabricated on land. Thereafter, these segments were floated and transported to the bridge site. The splitter plate was then attached to the back face of the steel caisson by welding, and was reinforced by diagonal truss. The finished structure is shown in Fig. 23.

## Concluding Remarks

While computations of the flow and hydrodynamic loads around rectangular cross-sectioned cylinders representative of caissons abound in the literature, none are available for a caisson at full scale and at realistic flow conditions leading to very high values of Reynolds number being attained. The need to provide reliable design data under these conditions provided the motivation for the present study. To establish the reliability of the data, simulations were performed using vastly different strategies to account for the effects of turbulence in the computations. The numerical accuracy of the computations was checked using the GCI method while verification was accomplished by comparisons with experimental data for a wide range of geometries and values of Reynolds number. Extensive computations were performed to determine the effectiveness of the two passive techniques of rounding the corners and of installing a base splitter plate in reducing both the mean and fluctuating lift and drag forces. Parametric studies were performed to determine the optimal value of $r/D$ in the case of rounded corners and the ratio $L/D$ for the splitter plate cases. The outcome of the computations was a recommendation that the caisson corners are to be rounded with a maximum allowable radius ration $r/D$ of $1/8.95$ (which translates to a radius of 2.1 m at full scale), and splitter plate length ratio $L/D$ of $1/10$ (which translates to a length of 2.94 m at full scale). These recommendations were implemented on an actual steel caisson during the construction of Boluo Dongjiang Bridge located in Guandong Province, South China. Reports from the field indicated that vortex shedding, as evidenced by the flow patterns on the surface, was entirely absent from the full-scale caisson with the recommended adaptations.

## Data Availability Statement

Some or all data, models, or code that support the findings of this study are available from the corresponding author upon reasonable request.

## Acknowledgments

## References

Bai, H. L., and M. M. Alam. 2018. "Dependence of square cylinder wake on Reynolds number." *Phys. Fluids* 30 (1): 015102. https://doi.org/10.1063/1.4996945.

Bearman, P. W., and E. D. Obasaju. 1982. "An experimental study of pressure fluctuations on fixed and oscillating square-section cylinders." *J. Fluid Mech.* 119 (Jun): 297–321. https://doi.org/10.1017/S0022112082001360.

Bruno, L., D. Fransos, N. Coste, and A. Bosco. 2010. "3D flow around a rectangular cylinder: A computational study." *J. Wind Eng. Ind. Aerodyn.* 98 (6–7): 263–276. https://doi.org/10.1016/j.jweia.2009.10.005.

Carassale, L., A. Freda, and M. Marre-Brunenghi. 2014. "Experimental investigation on the aerodynamic behavior of square cylinders with rounded corners." *J. Fluids Struct.* 44 (1): 195–204. https://doi.org/10.1016/j.jfluidstructs.2013.10.010.

Celik, I. B., U. Ghia, P. J. Roache, C. J. Freitas, H. Coleman, and P. E. Raad. 2008. "Procedure for estimation and reporting of uncertainty due to discretization in CFD applications." *J. Fluids Eng.* 130 (7): 078001. https://doi.org/10.1115/1.2960953.

Dai, S., B. A. Younis, and H. Y. Zhang. 2017. "Prediction of turbulent flow around a square cylinder with rounded corners." *J. Offshore Mech. Arctic Eng.* 139 (3): 031804. https://doi.org/10.1115/1.4035957.

Dai, S., B. A. Younis, H. Y. Zhang, and C. Y. Guo. 2018. "Prediction of vortex shedding suppression from circular cylinders at high Reynolds number using base splitter plates." *J. Wind Eng. Ind. Aerodyn.* 182 (Nov): 115–127. https://doi.org/10.1016/j.jweia.2018.09.006.

Durao, D. F. G., M. V. Heitor, and J. C. F. Pereira. 1998. "Measurements of turbulent and periodic flows around a square cross-section cylinder." *Exp. Fluids* 6 (1): 298–304. https://doi.org/10.1007/BF00538820.

Gerrard, J. H. 1966. "The mechanics of the formation region of vortices behind bluff bodies." *J. Fluid Mech.* 25 (2): 401–413. https://doi.org/10.1017/S0022112066001721.

Igarashi, T. 1997. "Drag reduction of a square prism by flow control using a small rod." *J. Wind Eng. Ind. Aerodyn.* 69 (Jul): 141–153. https://doi.org/10.1016/S0167-6105(97)00150-5.

Issa, R. I. 1986. "Solution of the implicitly discretised fluid flow equations by operator-splitting." *J. Comp. phys.* 62 (1): 40–65. https://doi.org/10.1016/0021-9991(86)90099-9.

Jeong, J., and F. Hussain. 1995. "On the identification of a vortex." *J. Fluid Mech.* 285 (1): 69–94. https://doi.org/10.1017/S0022112095000462.

Jones, D. A., M. Chapuis, M. Liefvendahl, D. Norrison, and R. Widjaja. 2016. *RANS simulations using OpenFOAM software*. Fishermans Bend, VIC, Australia Maritime Platforms Division, DST Group Defense Science and Technology Group.

Krishna, M. S., P. Chakrabarti, S. K. Chakrabarti, A. Mukkamala, and N. Anavekar. 2004. "Overview of Tacoma narrowsbridge floating caisson design." Vol. 1 of *Proc., 23rd Int. conf. Offshore Mechanics and Arctic Engineering, Vancouver, Canada*, 465–478. New York: ASME.

Lee, B. E. 1975. "The effect of turbulence on the surface pressure field of a square prism." *J. Fluid Mech.* 69 (2): 263–282. https://doi.org/10.1017/S0022112075001437.

Luo, S. C., M. G. Yazdani, Y. T. Chew, and T. S. Lee. 1994. "Effects of incidence and afterbody shape on flow past bluff cylinders." *J. Wind Eng. Ind. Aerodyn.* 53 (3): 375–399. https://doi.org/10.1016/0167-6105(94)90092-2.

Lyn, D. A. 1992. *Ensemble-averaged measurements in the turbulent near wake of a square cylinder: A guide to the data*. Rep. No. CE-HSE-92-6. West Lafayette, IN: School of Civil Engineering, Purdue Univ.

Lyn, D. A., S. Einav, W. Rodi, and J. H. Park. 1995. "A laser-Doppler velocimetry study of ensemble-averaged characteristics of the turbulent near wake of a square cylinder." *J. Fluid Mech.* 304 (10): 285–319. https://doi.org/10.1017/S0022112095004435.

Miran, S., and C. H. Sohn. 2015. "Numerical study of the rounded corners effect on flow past a square cylinder." *Int. J. Numer. Methods Heat Fluid Flow* 25 (4): 686–702. https://doi.org/10.1108/HFF-12-2013-0339.

Nakaguchi, H., K. Hashimoto, and S. Muto. 1968. "An experimental study on aerodynamic drag of rectangular cylinders." *J. Jpn. Soc. Aeronaut. Space Sci.* 16 (168): 1–5. https://doi.org/10.2322/jjsass1953.16.1.

Norberg, C. 1993. "Flow around rectangular cylinders: Pressure forces and wake frequencies." *J. Wind Eng. Ind. Aerodyn.* 49 (1–3): 187–196. https://doi.org/10.1016/0167-6105(93)90014-F.

Rathakrishnan, E. 1999. "Effect of splitter plate on bluff body drag." *AIAA J.* 37 (9): 1125–1126. https://doi.org/10.2514/2.823.

Saha, A. K., K. Muralidhar, and G. Biswas. 2000. "Experimental study of flow past a square cylinder at high Reynolds numbers." *Exp. Fluids* 29 (6): 553–563. https://doi.org/10.1007/s003480000123.

Sarioglu, M. 2017. "Control of flow around a square cylinder at incidence by using a splitter plate." *Flow Meas. Instrum.* 53 (B): 221–229. https://doi.org/10.1016/j.flowmeasinst.2016.06.024.

Sarioglu, M., Y. E. Akansu, and T. Yavuz. 2005. "Control of flow around square cylinders at incidence by using a rod." *AIAA J.* 43 (7): 1419–1426. https://doi.org/10.2514/1.9460.

Schlichting, H., and K. Gersten. 2017. *Boundary-layer theory*. 9th ed. Berlin: Springer-Verlag.

Shimada, K., and T. Ishihara. 2002. "Application of a modified model to the prediction of aerodynamic characteristics of rectangular cross-section cylinders." *J. Fluids Struct.* 16 (4): 465–485. https://doi.org/10.1006/jfls.2001.0433.

Smagorinsky, J. 1963. "General circulation experiments with the primitive equations. I: The basic experiment." *Mon. Weather Rev.* 91 (3): 99–164. https://doi.org/10.1175/1520-0493(1963)091<0099:GCEWTP>2.3.CO;2.

Sohankar. 2006. "Flow over a bluff body from moderate to high Reynolds numbers using large eddy simulation." *Comput. Fluids* 35 (10): 1154–1168. https://doi.org/10.1016/j.compfluid.2005.05.007.

Tamura, T., and T. Miyagi. 1999. "The effect of turbulence on aerodynamic forces on a square cylinder with various corner shapes." *J. Wind Eng. Ind. Aerodyn.* 83 (1–3): 135–145. https://doi.org/10.1016/S0167-6105(99)00067-7.

Tamura, T., T. Miyagi, and T. Kitagishi. 1998. "Numerical prediction of unsteady pressures on a square cylinder with various corner shapes." *J. Wind Eng. Ind. Aerodyn.* 74 (Apr): 531–542. https://doi.org/10.1016/S0167-6105(98)00048-8.

Vickery, B. J. 1966. "Fluctuating lift and drag on a long cylinder of square cross-section in a turbulent stream." *J. Fluid Mech.* 25 (3): 481–494. https://doi.org/10.1017/S002211206600020X.

Wang, X., and M. Gu. 2015. "Experimental investigation of Reynolds number effects on 2D rectangular prisms with various side ratios and rounded corners." *Wind Struct.* 21 (2): 183–202. https://doi.org/10.12989/was.2015.21.2.183.

Wang, X., and M. Gu. 2016. "Experimental study on wind pressure distributions of 2-D square prisms with various corner treatments." *China Civ. Eng. J.* 49 (7): 79–88. https://doi.org/10.15951/j.tmgcxb.2016.07.007.

Yakhot, V., and S. A. Orszag. 1986. "Renormalization group analysis of turbulence. I. Basic theory." *J. Sci. Comp.* 1 (1): 3–51. https://doi.org/10.1007/BF01061452.

Yakhot, V., S. A. Orszag, S. Thangam, T. B. Gatski, and C. G. Speziale. 1992. "Development of turbulence models for shear flows by a double expansion technique." *Phys. Fluids A* 4 (7): 1510–1520. https://doi.org/10.1063/1.858424.

Yang, H., S. Hou, W. Yang, S. Li, H. Hou, and Q. Li. 2022. "Experimental investigation of current forces on a square caisson with small aspectratios during the sinking process." *J. Hydraul. Res.* 60 (6): 959–969. https://doi.org/10.1080/00221686.2022.2106588.

Yang, H., W. Yang, Q. Li, and J. Kou. 2019. "Experimental investigation of current forces on floating cylinder during the sinking process." *Ocean Eng.* 178 (Apr): 134–144. https://doi.org/10.1016/j.oceaneng.2019.02.060.

Younis, B. A., and V. Przulj. 2006. "Computation of turbulent vortex shedding." *Comput. Mech.* 37 (5): 408–425. https://doi.org/10.1007/s00466-005-0713-2.